ELSEVIER

Journal of Fluids and Structures 24 (2008) 129–150

JOURNAL OF FLUIDS AND STRUCTURES

www.elsevier.com/locate/jfs

# Dynamic stall behavior from unsteady force measurements

K.K.Y. Tsang, R.M.C. So, R.C.K. Leung*, X.Q. Wang

*Department of Mechanical Engineering, The Hong Kong Polytechnic University, Hung Hom, Kowloon, Hong Kong*

Received 11 October 2006; accepted 22 June 2007

**Abstract**

A direct force measurement technique employing piezoelectric load cells is used to experimentally investigate a two-dimensional airfoil (NACA 0012) undergoing dynamic stall. The load cells are installed at each end of the airfoil and give the force response in two directions in the plane normal to the airfoil axis during oscillations. Experiments are carried out at a Reynolds number based on the airfoil chord equal to $7.7 \times 10^4$, and at four reduced frequencies, $k = 0.005$, 0.01, 0.02, and 0.04. Phase-averaged lift of the airfoil undergoing dynamic stall is presented. It is observed that hysteresis loops of the lift occur both when the airfoil is pitched to exceed its static stall limit and when it is still within its static stall limit, and they grow in size with increasing $k$ at the same pitching mean angle of attack and pitching amplitude. Both the lift and the drag induced by the pitching motion are further analyzed using the methods of higher order correlation analysis and continuous wavelet transforms to undercover their nonlinear and nonstationary features, in addition to classical FFT-based spectral analysis. The results are quantitatively illustrated by an energy partition analysis. It is found that the unsteady lift and drag show opposite trends when the airfoil undergoes transition from the pre-stall regime to the full-stall regime. The degree of nonlinearity of the lift increases, and the lift show a nonstationary feature in the light-stall regime, while the nonlinearity of the drag decreases, and the drag shows nonstationary feature in both the light-stall and the full-stall regimes. Furthermore, the lift and the drag have significant nonlinear interactions as shown by the correlation analysis in the light-stall regime.
© 2008 Elsevier Ltd. All rights reserved.

## 1. Introduction

When an airfoil undergoes a rapid increase in the angle of attack, large overshoots in lift, drag, and pitch moment take place. Loss of lift will occur, and lift and moment stall are delayed to higher angles of attack compared to quasi-steady stall values. This phenomenon is referred to as "dynamic stall". When dynamic stall occurs, the flow separates from the airfoil, and the loss of lift is more abrupt and more persistent than that of static stall. Once the flow is separated, reattachment takes place only when the airfoil is pitched down to an angle of attack, $\alpha$, much lower than the static stall angle, $\alpha_{ss}$, or when the airfoil is being pitched up again. Owing to this large hysteresis in the flow development, dynamic stall is accompanied by large phase variations in the unsteady air load. Hence, the value of the unsteady air load is dependent on whether the flow is separating, fully separated, or reattached (Leishman, 2000). Furthermore, it is believed that dynamic stall is related to the formation, development, and shedding of a leading-edge vortex (Carr, 1998).

*Corresponding author. Tel.: +852 2766 6645. fax: +852 2766 4703.
*E-mail address:* mmrleung@inet.polyu.edu.hk (R.C.K. Leung).

0889-9746/$ - see front matter © 2008 Elsevier Ltd. All rights reserved.
doi:10.1016/j.jfluidstructs.2007.06.007

Experimental investigations have been conducted to examine the aerodynamics associated with dynamic stall and its delay, as well as the influence of stall parameters on the dynamic stall process and its characteristics (Carr et al., 1977; McAlister et al., 1978; Carr, 1998). Some of the more important parameters investigated are: airfoil geometry, mean angle of attack and the amplitude of oscillation, reduced frequency, $k = \pi fc/U_\infty$, Reynolds number, $\mathrm{Re} = U_\infty c/\nu$, and Mach number, $M = U_\infty/a$, where $f$ is the pitching frequency in Hz, $c$ is the airfoil chord length, $a$ is the speed of sound, and $U_\infty$ is the free stream velocity. Some of the commonly used experimental techniques to study dynamic stall behavior include surface pressure measurement using pressure transducers (Walker et al., 1985; Albertson et al., 1987; Conger and Ramaprian, 1994; Piziali, 1994), flow velocity measurement around the airfoil using constant temperature anemometry (CTA) or laser Doppler anemometry (LDA), and velocity field measurement using particle image velocimetry (PIV) (Panda and Zaman, 1992, 1994; Oshima and Ramaprian, 1992; Wernert et al., 1996). The force and moment response of the oscillating airfoil are often computed from the measured surface pressure and vorticity data. In other studies, researchers employed a combination of different measuring techniques to study the various characteristics of the dynamic stall process (Martin et al., 1974; Carr et al., 1977; Panda and Zaman, 1994).

When an airfoil is oscillating sinusoidally as in most dynamic stall studies, energy is constantly input to the airfoil by the pitching motion. Since the motion is periodic, numerous studies investigate the phenomenon by examining the phase-averaged values of the lift. The implicit assumption is that the measured lift is time-stationary in a periodic sense. However, this assumption might not be able to stand up to scrutiny. Besides, despite the impressive progress made on the understanding of the dynamic stall phenomenon, scant attention has been placed on the investigation of the frequency content of the lift and drag signal of a two-dimensional (2-D) airfoil undergoing dynamic stall, which is associated with the energy content of the structure. If the frequency content of the unsteady lift and drag signal and the stationary nature of the aerodynamic response of the pitching airfoil were to be examined, the force needs to be measured directly.

Since most force data is deduced from the measured surface pressure or vorticity, integration of the measured quantity is required in order to determine the lift and drag force. Irrespective of the frequency content of the measured signals, when integration is invoked, high frequency components of the signal are filtered out and only low frequency components are left in the resultant force signals. Therefore, certain important information concerning the behavior of the fluctuating force could be lost. Compared to indirect techniques, direct force measurement can better capture the actual aerodynamic response of the test model. Besides, the frequency content of the measured signal is limited by the test model and by the frequency response of the measuring equipment, such as sensors and amplifiers. The aerodynamic response can be recorded as an analog or a digitized signal. Of course, the resolvable frequency range of the digitized signal will depend on the sampling rate. Either way, the raw force signal could be stored for later analysis without lost of information.

In the past, direct measurements of the mean and fluctuating force acting on rigid and elastic structures are carried out using one of several available methods; pressure transducers or balance method for mean force measurements, and resistance-wire strain gauge for fluctuating force measurements. The strain gauge technique has one drawback though; in order to ensure reliably measurable strain the structure needs to be sufficiently flexible. This conflicts with the requirement that the structure has to be rigid, or there is a danger of the results being contaminated by the structural dynamics.

With the development of piezoelectric load cells, the technique has been used by researchers to measure fluctuating forces because they do not suffer the same drawbacks as resistance-wire strain gauges. A piezoelectric load cell has been employed to successfully measure the spanwise-averaged Strouhal force on circular cylinders (Richter and Naudescher, 1976). The study shows that the technique can resolve the mean and root mean square (rms) force in both the lift and drag direction together with their dominant frequencies. Thus, the experiment is able to show that the dominant drag force frequency is twice that of the lift. The measurements not only give the mean and fluctuating forces but also the statistics and the frequency content of the force signals. The technique is later used to measure the buffeting force on cylinders in a cross-flow in order to resolve the full spectra of the fluctuating lift and drag (Savkar et al., 1980; So and Savkar, 1981). This technique is further extended to study the fluctuating forces on cylinder arrays (Lam et al., 2003) and on wavy cylinders (Lam et al., 2004). Since then, improvements have been made to the technique so that it can be used to measure local fluctuating forces on 2- and 3-D cylinders (Sin and So, 1987; Baban et al., 1989). The modified technique has been used to study the correlation between unsteady forces and the wake flow behind finite cylinders (Baban and So, 1991).

The load cell technique has also been extended to study dynamic stall where the load cell is used to measure the unsteady forces acting on an oscillating airfoil (Zaman et al., 1989). However, it is found that the technique is only successful when the oscillation amplitude is small and the mean pitching angle is $\alpha \approx 0^\circ$. This is by no means an indication of the inadequacy of the load cells. Rather, it could be attributed to inadequacy in the design of the airfoil test model. A recent study of insect flight behavior using a load cell has essentially confirmed that it could be used to

measure unsteady forces acting on the wings of a model fruit fly (Dickinson et al., 1999). The test model is driven by an assembly of six computer-controlled stepper motors attached to a wing gearbox via timing belts and coaxial drive shafts; each of the two wings is capable of rotational motion about three axes. Therefore, the model is capable of yielding direct measurements of the time history of the aerodynamic force in two directions, and the three interactive mechanisms of insect flight; namely the delayed stall (dynamic stall), the rotational circulation, and the captured wake.

The fruit fly study shows that piezoelectric load cells can be used to measure the unsteady forces acting on wings undergoing dynamic stall, thereby allowing the unsteady force behavior to be examined in detail. This means that with a properly designed airfoil test model, the load cell technique can be used to examine dynamic stall where the amplitude of oscillations and the mean angle of attack are not necessarily small. An attempt to design an airfoil model with appropriate improvements to study dynamic stall where the mean pitching angle varies from $0^\circ$ to $15^\circ$ and the oscillation amplitude could be as large as $10^\circ$ has been carried out (Tsang, 2006). In that study, the measured dynamic stall behavior is qualitatively corroborated by flow visualization study wherever possible.

The present study makes use of the improved technique to measure the unsteady force induced on a 2-D airfoil undergoing dynamic stall at low Re. The focus of the paper is on analyzing the force behavior using data analysis techniques, such as higher order correlation analysis and continuous wavelet analysis, to scrutinize the measured unsteady force data.

## 2. Experimental set-up

Details of the complete experimental set-up are given in Tsang (2006). However, for the sake of completeness, the closed-circuit wind tunnel used to carry out the experiment, the design criteria for the 2-D airfoil model, the airfoil model thus designed and fabricated, and the technique used to deduce the force normal to and along the chord is briefly described below. Finally, the conditions of the dynamic stall experiments are specified.

### 2.1. Wind tunnel facility and flow around the airfoil

All force measurement experiments are carried out in a closed-circuit subsonic wind tunnel which has a square test-section of 600 mm × 600 mm. The length of the test-section is 2.4 m and the contraction ratio of the wind tunnel is 9:1. The wind tunnel can produce a maximum flow speed of 40 m/s at the test-section. Turbulence intensity is 0.03% measured at a free stream velocity of 18.8 m/s and increases slowly with $U_\infty$. The airfoil model together with the pitching mechanism and load cells is mounted across the test-section at 0.46 m downstream of the test-section entrance; its design and fabrication are discussed in detail in Tsang (2006). In order to establish a 2-D flow around the airfoil, end-plates are installed at both ends of the airfoil to minimize the effect of wall boundary layer buildup and its influence on the spanwise development of the flow around the airfoil. The $xyz$ coordinate system is attached to the airfoil trailing edge at mid-span, where $x$ is the stream direction, $y$ is the transverse direction, and $z$ is the span direction (Fig. 1).

In order to ascertain the 2-D nature of the flow, constant temperature hot-wire anemometer is used to carry out the velocity measurements along the span of the airfoil. A Dantec Model 55P51 gold-plated X-wire probe is used to measure the velocity components ($u$ and $v$) along the $x$- and $y$-direction. The probe has two 5-μm-diameter 3-mm-long platinum-plated tungsten wire sensors. This X-wire probe can resolve velocities from 0.2 to 200 m/s. The frequency

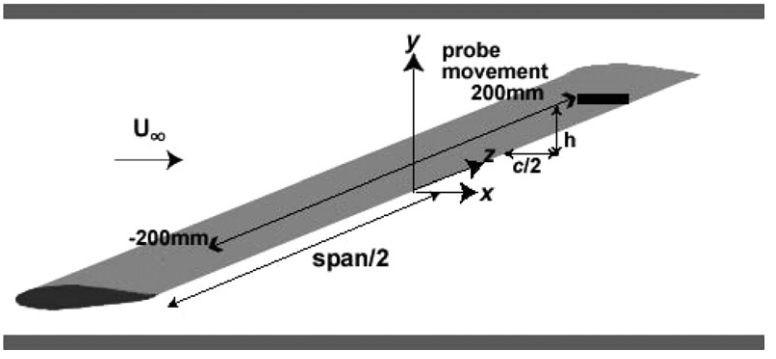


Fig. 1. Airfoil model setup in the test-section and the coordinate system.

response is 90 kHz at 100 m/s. Calibration of the hot-wire is carried out by placing the X-wire probe in the middle of the test-section at the location where the airfoil is mounted and varying the flow speed of the wind tunnel. The calibration curves thus obtained are found to be quite repeatable with essentially no change in the slope of the voltage versus velocity square curve (Tsang, 2006).

The 2-D nature of the flow around the airfoil needs to be established and the objective is to determine to what extent $v = 0$ and $u$ is uniform across the $y$- and $z$-direction. The entrance flow across the $y$- and $z$-direction is essentially uniform with $v \approx 0$. Velocity components $u$ and $v$ along the span of the airfoil are measured at $c/4$ downstream of the trailing edge. The width of the wake at mid-plane of the airfoil at $x = c$ is measured by traversing the flow along the $y$-direction. A $y$ location where $u$ is essentially the same as $U_\infty$ is determined from this measurement for each angle of attack $\alpha$. The X-wire probe is then positioned at this $(x, y)$ location to measure $u$ and $v$ along the airfoil span with $s = 400$ mm (Fig. 1). The digitized data is collected using a 16-channel, 12-bit A/D board. The sampling rate is 400 Hz and the sample length is 10 s for all $\alpha$ tested. This is long enough to give a mean $u$ and $v$ that does not vary with time. Results obtained for fixed $\alpha = 0^\circ$, $3^\circ$, $6^\circ$, $8^\circ$, $9^\circ$, and $12^\circ$ without pitching show that the mean $v \approx 0$ for all $\alpha$ measured and the spanwise variation of the mean $u$ normalized by its value at mid-span is less than 3% for $\alpha < \alpha_{ss}$ but increases to about 5–6% for $\alpha > \alpha_{ss}$. The greatest variation occurs near the end-plates of the airfoil. The variation along the central 75% span is less than 1% for all $\alpha$ tested; therefore, the flow along the central span of the airfoil can be said to be essentially 2-D.

### 2.2. Design criteria for the 2-D airfoil model

The design criteria for the 2-D airfoil are specified as follows. First, the airfoil model has to have a pitching mechanism built in so that the airfoil will not twist as a result of pitching, and bending is essentially zero. Second, the load cells should move with the airfoil so that they can measure the instantaneous force directly in the direction normal to and along the chord of the airfoil. Third, the airfoil has to be relatively stiff so that the natural frequency is far removed from the dominant frequency of dynamic stall. Fourth, the mounting of the airfoil at both ends should be identical, so that 2-D flow around the airfoil could be maintained. Finally, the dynamic range of the whole setup has to be reasonably high to capture the high frequency components of the dynamic stall force signals.

In the past, most experimental studies mounted the oscillating airfoil at one end, where the oscillating mechanism is also installed. This means that one end of the airfoil model is connected to the pitching mechanism directly, while the other end of the airfoil is either supported by a bearing or the airfoil is simply mounted as a cantilever with a small gap between the test-section wall and the airfoil. Either way, this type of mounting yields a mixed boundary condition for the test model; a fixed-end and a simply supported (or free end) boundary condition. Under this mixed boundary condition, the 2-D flow around the airfoil could be compromised because the airfoil is not completely rigid. Pitching an airfoil with only one end mounted therefore relies on the structural stiffness of the model to transfer the pitching moment to the other end. However, in reality, all structures have finite stiffness. Therefore, the 2-D flow condition is approximately satisfied if and only if the airfoil is not in motion. Previous study has shown that the rigidity assumption is an approximation and torsional deformation of the model could result (Lau et al., 2004). Consequently, the force data obtained will be contaminated by 3-D flow effects (So et al., 2005).

In view of this, the airfoil model should be designed to have a driving mechanism to oscillate the airfoil at both ends, where force cells are also installed to measure the spanwise-averaged lift and drag force. The driving mechanisms should be located outside of the wind tunnel and not attached to its sidewalls in order to avoid signal contamination by tunnel wall vibrations. This way, the weight of the two driving mechanisms is carried by a separate frame and the airfoil is free to oscillate without fear of twisting and bending. Furthermore, the load cells will move with the pitching airfoil and always measure the force components normal to and along the chord of the airfoil. If the model is designed properly, the load cell at each end of the airfoil measures one half the spanwise-averaged lift and drag force and together they will give the total lift and drag force acting on the airfoil (Savkar et al., 1980; So and Savkar, 1981).

### 2.3. Mounting of the 2-D airfoil model and force measurements

A schematic showing the airfoil, the servomotors and the load cells is given in Fig. 2. The geometry of the 2-D model is a NACA 0012 airfoil with a chord, $c = 0.06$ m and a span $s = 0.4$ m (measured from end-plate to end-plate). The airfoil is fabricated using carbon fiber and built around a shaft located at the quarter-chord point. Two low-inertia AC servomotors are used to oscillate the airfoil about this shaft. A programmable logic controller is used to control the motors. Each motor is programmed to pitch the airfoil sinusoidally and simultaneously at each end.

Two Kistler Type 9251A three-component piezoelectric load cells are used to directly measure the unsteady forces acting on the airfoil. For ease of reference, the three directions are designated as $X$, $Y$, and $Z$ where $X$ and $Y$ lie in the

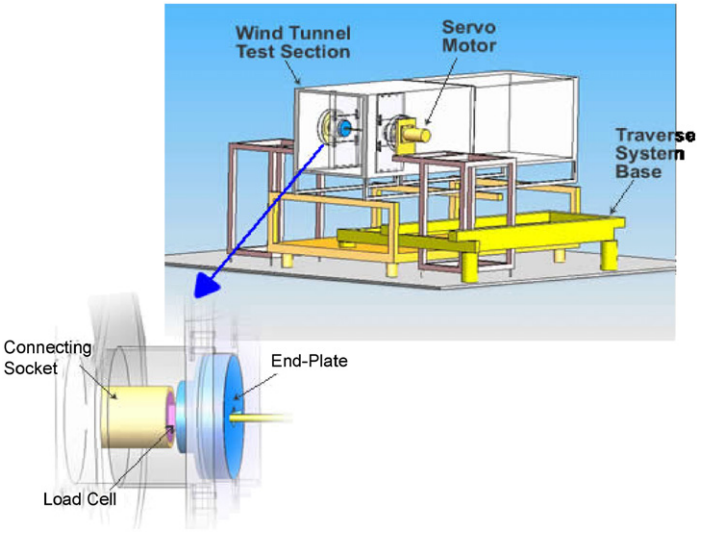


Fig. 2. Airfoil model and the associated mountings for the load cells.

plane of the load cell sensor and $Z$ normal to the $XY$ plane. The load cell measures the tensile force when the applied force is in the direction of the load cell axis, and the shear force when the applied force is perpendicular to load cell axis. Since friction is the only mechanism used to transmit shear force in the load cell, a preloading must be applied. For the present application, the load cell is installed in the airfoil model so that its axis ($Z$-axis) coincides with the airfoil axis passing through its quarter-chord point. A preload is applied along the $Z$-axis. Thus installed, the load cell measures the resultant (lift and drag) force whose direction is normal to the $Z$-axis. In order to ensure linearity of the charge output of the force measured and hence the accuracy of the measurements, a preload-to-maximum measured load ratio of 10 is recommended by the manufacturer. For the present experiments, a preload of 13 kN is applied to the load cells through the installation of a Kistler Type 9461 preloading set and two stainless steel circular plates. Since the maximum force measured is less than 15 N, the magnitude of the preload is more than sufficient for the present purpose.

Two separate frames are fabricated to mount the motors on each side of the test-section so that they are not in contact with the test-section walls. This is to prevent the force signals from being contaminated by tunnel wall vibrations. The NACA 0012 airfoil model with an end-plate at each end is mounted horizontally at the mid-plane of the test-section. One of the pre-load plates is housed inside the end-plate at each end of the airfoil (Fig. 2). The other pre-load plate of the load cell is housed inside a connecting socket, one at each end of the airfoil model. The two connecting sockets are then installed onto the motor shaft. This airfoil assembly gives a clamped–clamped boundary condition. When the airfoil is pitched, the load cells installed at the two ends rotate with the airfoil. Thus designed, the two axes of each load cells measure the force normal to and along the chord of the airfoil.

The load cells output electrical charges that are linearly proportional to the shear force measured in the $X$- and $Y$-direction. Four Kistler Type 5011B charge amplifiers are used to convert the electrical charges from the load cells into a proportional voltage signal. Each charge amplifier has an upper frequency limit of 200 kHz and is equipped with an adjustable eight-stage low-pass filter which allows reduction of the upper frequency limit. The voltage signals output by the charge amplifiers are then input to a data acquisition system. The signal length collected is more than 10 cycles for each pitching frequency; only 10 cycles are used for data analysis though.

### 2.4. Load cell calibrations

Static calibration using dead weights is carried out for the $X$- and $Y$-axis separately in a frame built to support the airfoil model assembly. It is found that the output voltages vary linearly with increasing weights; the calibration curves thus obtained for the two load cells are very repeatable and the slopes of the curves remain essentially the same over time (Tsang, 2006). Impulse tests in still air are conducted to determine the natural frequency of the airfoil by measuring the vibration amplitude using a laser vibrometer. Again, the airfoil assembly is mounted in a separate frame outside of the wind tunnel. A schematic of the impulse test set-up is shown in Fig. 3(a). A sample plot of the power spectrum calculated from the displacement signal measured from the impulse test of the airfoil is shown in Fig. 3(b). It can be seen

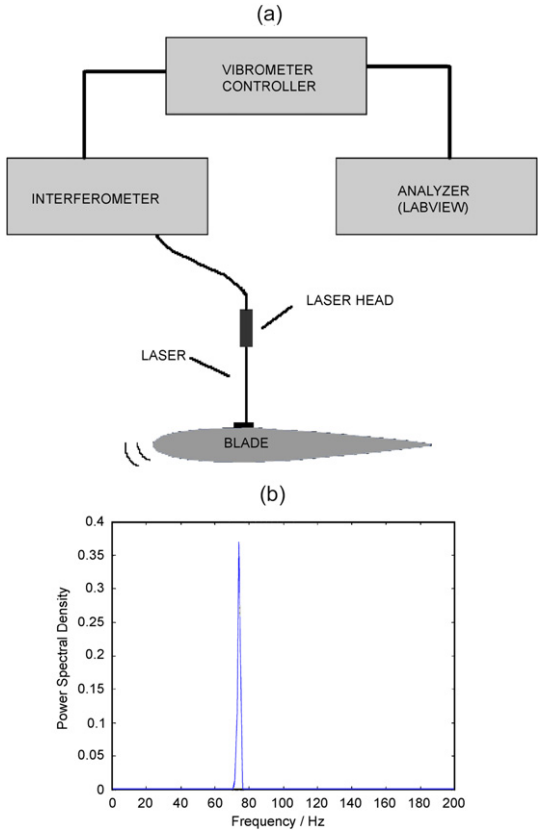


Fig. 3. Calibration set-up for the airfoil model: (a) schematic of the airfoil and laser vibrometer arrangement; (b) PSD of the measured lift.

that a very prominent peak is observed in the plot and the frequency at which the peak occurs is taken to be the first mode natural frequency $f_n$, which is ~75 Hz.

### 2.5. Experimental conditions

All experiments are carried out with $U_\infty = 18.8$ m/s and a $\mathrm{Re} = 7.7 \times 10^4$. This is the maximum possible speed where the free stream turbulence is $\leqslant 0.03\%$. This relatively high flow speed is selected to maximize the signal to noise ratio of all load cell outputs and to give the highest possible low Re. With $c = 0.06$ m, the maximum blockage is 10% at $\alpha = 30^\circ$.

Steady force measurements are obtained first. With the current set-up, it is found that it only takes 2 s of data to determine a reliable value for the steady force. Hence, by properly controlling the motors, the airfoil is pitched from $\alpha = -8^\circ$ to $30^\circ$ at $1^\circ$ increments. At each angle of attack the airfoil is held for 5 s and steady force measurements are taken. The static stall angle is determined to be around $10^\circ$. Therefore, the following experimental cases are chosen. Two oscillation cases, which are Case 1: $\alpha = 0^\circ + 5^\circ \sin(\omega t)$ and, Case 2: $\alpha = 5^\circ + 5^\circ \sin(\omega t)$, are selected within the pre-stall region; two oscillation cases which are Case 3: $\alpha = 10^\circ + 5^\circ \sin(\omega t)$ and Case 4: $\alpha = 10^\circ + 10^\circ \sin(\omega t)$ are selected in the light-stall region; and one oscillation case which is Case 5: $\alpha = 15^\circ + 10^\circ \sin(\omega t)$ is selected in the full-stall region of the airfoil. Here, $\omega$ is the angular pitching frequency. Four reduced frequencies, $k = 0.005$, 0.01, 0.02, and 0.04, are tested for each case.

## 3. Results and discussion

The primary focus of this paper is on the use of various data analysis techniques to examine dynamic stall behavior and the vehicle is the measured fluid force (lift and drag) signals. The emphasis will be put on the nonlinear and

nonstationary behavior of the lift and the drag force when the airfoil undergoes dynamic stall at low Re. The experiment is carried out at $\mathrm{Re} = 7.7 \times 10^4$. Therefore, the steady lift measurements are first discussed with an objective to show that the theoretical lift curve slope is recovered at this Re. This is followed by a discussion of the unsteady lift measurements and the effect of reduced frequency on its maximum value. Finally, the stationary/nonstationary and linear/nonlinear behavior of the lift and drag data are discussed using the energy partition results derived from spectral analysis, wavelet analysis results, and coherence functions.

### 3.1. Pre-processing of data

During each run of the force measuring experiments, the time series of five signals are recorded. These include the voltage signals from the $X$- and $Y$-axes of each load cell and an analog position reference signal of the motor shaft. All data are sampled at a rate of 1000 Hz. Voltage signals from the load cells are passed through a 300 Hz low-pass filter and the filtered signals are converted to force signal separately using appropriate calibration curves. The normal force, measured by the $Y$-axis of the load cells, and the chord-wise force, measured by the $X$-axis of the load cells, are resolved to give the time series of the lift and drag force acting on the airfoil. In view of the low-pass filtering of the force signals, the maximum frequency that can be resolved in the lift and drag components is 300 Hz. This range is four times the static natural frequency of the airfoil.

The force signals measured during the wind-on tests consist of both the aerodynamic and inertia force. Thus, it is necessary to determine the inertia force arising from its oscillatory motion under wind-off condition. Aerodynamic force responses are obtained by subtracting the signals measured under wind-off conditions from those measured under wind-on conditions. Thus, time series of the spanwise-averaged lift and drag and their associated coefficients undergoing pitching motion are obtained. Phase averaging of the force data so obtained is then carried out to better characterize the aerodynamic responses as a function of $\alpha$. According to the instantaneous reference position signal, 10 oscillations of each set of data are extracted and used to carry out the averaging. For illustration purposes, only the lift variation with the instantaneous $\alpha$ for Cases 2 and 5 are shown in Fig. 4(a) and (b), respectively, while those for the drag are not shown. Therefore, the recorded data for each cycle will show the airfoil beginning with the minimum $\alpha$, pitch up to the maximum $\alpha$, and then return to the minimum $\alpha$.

Furthermore, it should be noted that when an airfoil undergoes oscillation in a fluid, additional pressure forces are required to accelerate the fluid in the vicinity of the airfoil (Leishman, 2000). This additional force is called the "apparent mass effect". From Theodorsen's theory, the apparent mass effect of a thin airfoil undergoing pitching only motion is given by

$$L_{\text{apparent}} = \pi\rho V^2 b\left[\frac{b}{U_\infty}\dot{\alpha} - \frac{b^2}{U_\infty}a\ddot{\alpha}\right], \tag{1}$$

where $a$ is the pitch axis location relative to the mid-chord of the airfoil, which is $(-1/2)$ in this case, $b$ is half-chord, and $\rho$ is air density. In order to assess the apparent mass effect on the measurements of the present study, the lift due to apparent mass is computed for Case 5 at $k = 0.04$ and the results are shown in Fig. 4(c) and (d) This case is chosen for its high $\alpha_{\text{mean}}$ and $\alpha_{\text{amp}}$ because of its relatively high reduced frequency. Fig. 4(c) shows both the time series of the net $C_l$ and the net $C_l$ after it has been corrected for the apparent mass effect. Fig. 4(d) shows the corrected net $C_l$ normalized by half of the maximum net $C_l$ of the time series. It can be seen that the apparent mass effect is at most 2% of half of the maximum net $C_l$, thus it is considered negligible in the present analysis and no apparent mass effect correction has been made to the lift data reported in this paper.

### 3.2. Steady lift behavior

The results of the steady lift coefficient ($C_l$) measurement are shown in Fig. 5. Lift increases progressively with $\alpha$ and with a slope equal to the theoretical slope of $2\pi$. It is clear that stall occurs at $\alpha \cong 10^\circ$ (Fig. 5). At first glance, this static stall angle seems to be small compared to others reported in the literature (Martin et al., 1974; Carr et al., 1977). However, it should be pointed out that the Re for these other experiments ($10^5 < \mathrm{Re} < 10^6$) are much higher than the present Re. According to Leishman (2000), inertial effects in the flow increase with Re; they dominate over the viscous effect and thin out the boundary layer at higher Re. In other words, the flow has more energy to overcome the momentum deficit created by viscosity. Consequently, the onset of flow separation is delayed to a higher $\alpha$ and a higher lift coefficient is measured at stall (Mary and Sagaut, 2002). Therefore, a higher static stall angle of the same airfoil ($\alpha_{ss} = 15^\circ$) is observed at higher Re as reported in most literature. Since the present experiments are conducted at $\mathrm{Re} = 7.7 \times 10^4$, a measured $\alpha_{ss} \approx 10^\circ$ is reasonable. This value is quite consistent with that reported by White (1979).

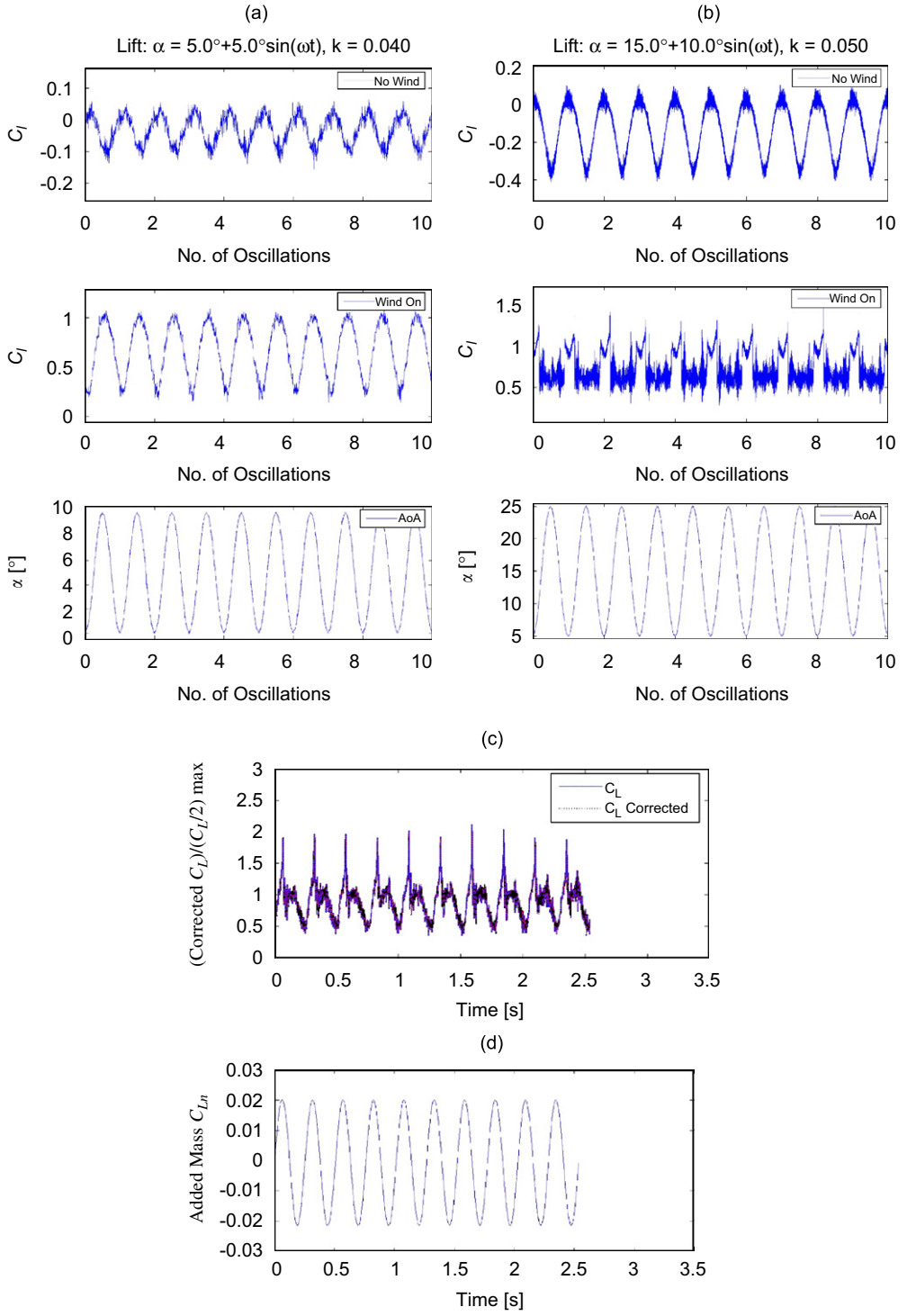


Fig. 4. Lift time series under wind-off and wind-on conditions and comparison of variation of corrected and uncorrected $C_l$ with time: (a) Case 2 with $k = 0.04$; (b) Case 5 with $k = 0.005$; (c) net $C_l$ compared with net $C_l$ corrected for apparent mass effect for Case 5; (d) net $C_l$ corrected for apparent mass and normalized by maximum net $C_l/2$ for Case 5.

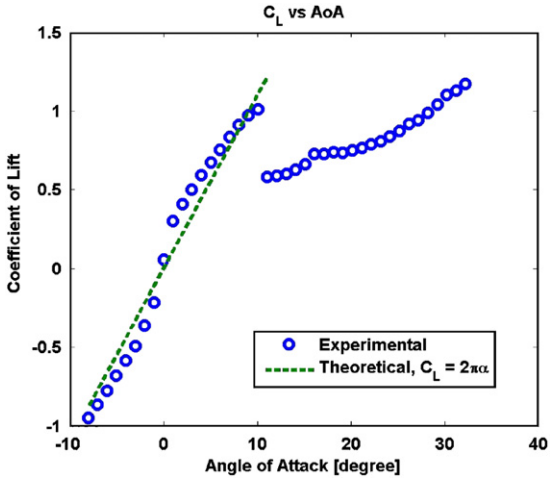


Fig. 5. A plot of the measured steady lift versus angle of attack for $-10^\circ \leqslant \alpha \leqslant 30^\circ$.

### 3.3. Unsteady lift behavior

The true instantaneous lift signals for Cases 2, 3, and 5 are shown in Fig. 6(a)–(c). These plots give the variation of the instantaneous lift coefficient $C_l$ with the instantaneous $\alpha$ of the airfoil. There are four panels in each figure and each is for one reduced frequency $k$. The effects of $k$ on $C_l$ variation are quite similar for Cases 3–5 investigated (see Fig. 6(b) and (c)). The behavior for Cases 1 and 2 is essentially the same, but it is different from Cases 3 to 5. In these figures, the measured static lift curve is plotted as a reference. The static lift curve is found consistent with Theodorsen's theory (Leishman, 2000). In addition, the phase-averaged lift curves for Case 2 (Fig. 6(a)) are in qualitative agreement with it. As $k$ increases, the lift plots evolve into counterclockwise hysteresis loops with the instantaneous lift lower than the steady value when the pitching is upward and higher than the steady value when the pitching is downward. When dynamic stall occurs as observed in Cases 3–5, the lift stalls at an angle higher than the static stall angle $\alpha_{ss}$, and remains this status until the airfoil is pitched down to an angle lower than $\alpha_{ss}$, at which time the lift readjusts to its pre-stall level. During dynamic stall, a significant increase in $C_l$ is first observed, followed by an equally abrupt drop.

### 3.4. Effect of k on the unsteady lift

The pitching motion depends on three parameters: the mean angle, the amplitude of the oscillation and the frequency of oscillation or $k$. Having a qualitative picture of dynamic stall behavior during one pitching cycle for three representative cases (Fig. 6(a)–(c)), the next step is to investigate the effect of these three parameters quantitatively. To this end, plots of the dynamic stall angle and the maximum value of lift coefficient ($C_{l\max}$) versus $k$ are shown in Fig. 7(a) and (b), respectively.

From Fig. 7(a), it can be observed that the stall angle increase as $k$ increases, but not in a linear way except for Case 4. An increase in the delay of the stall angle with $k$ is also noted, although the increase may not be significant in some cases, e.g., Case 5 with $k = 0.005$ and 0.01. Meanwhile, the angle at which the unsteady lift coefficient $C_l$ returns to its pre-stall value is also delayed, and this delay increases with $k$. It should be noted, however, that $C_l$ does not recover to its pre-stall value for the remainder of the down-stroke in some cases, such as Case 5 with $k = 0.02$ and 0.04.

On the other hand, $k$ has little or no effect on $C_{l\max}$ when the airfoil is in the pre-stall regime, as shown by the curves for Cases 1 and 2 in Fig. 7(b). Once $\alpha$ has passed $\alpha_{ss}$, dynamic stall occurs and increasing $k$ gives rise to increasing $C_{l\max}$, as shown by the curves for Cases 3–5 in Fig. 7(b). The increase is essentially linear for the three stall cases studied; however, the slope for Case 3 is much smaller than those for Cases 4 and 5, which are approximately identical.

Having examined the effect of $k$, it would be educational to study the effect of $\alpha_{mean}$ and $\alpha_{amp}$ on dynamic stall. These latter two parameters determine the excursion of the airfoil beyond $\alpha_{ss}$ before stall actually occurs. Two cases have the same $\alpha_{amp}$ but different $\alpha_{mean}$; they are Cases 4 and 5. As shown in Fig. 7(a) and (b), $\alpha_{mean}$ has a slight effect on the dynamic stall angle and little or no effect on $C_{l\max}$. The result indicates that for Case 5 where $\alpha_{mean}$ is larger, the dynamic stall angle is smaller at the same $k$. There are also two stall cases where $\alpha_{mean}$ is the same but $\alpha_{amp}$ is different. These are Cases 3 and 4. It is clear from Fig. 7(a) and (b) that $\alpha_{amp}$ has an effect on both the dynamic stall angle and

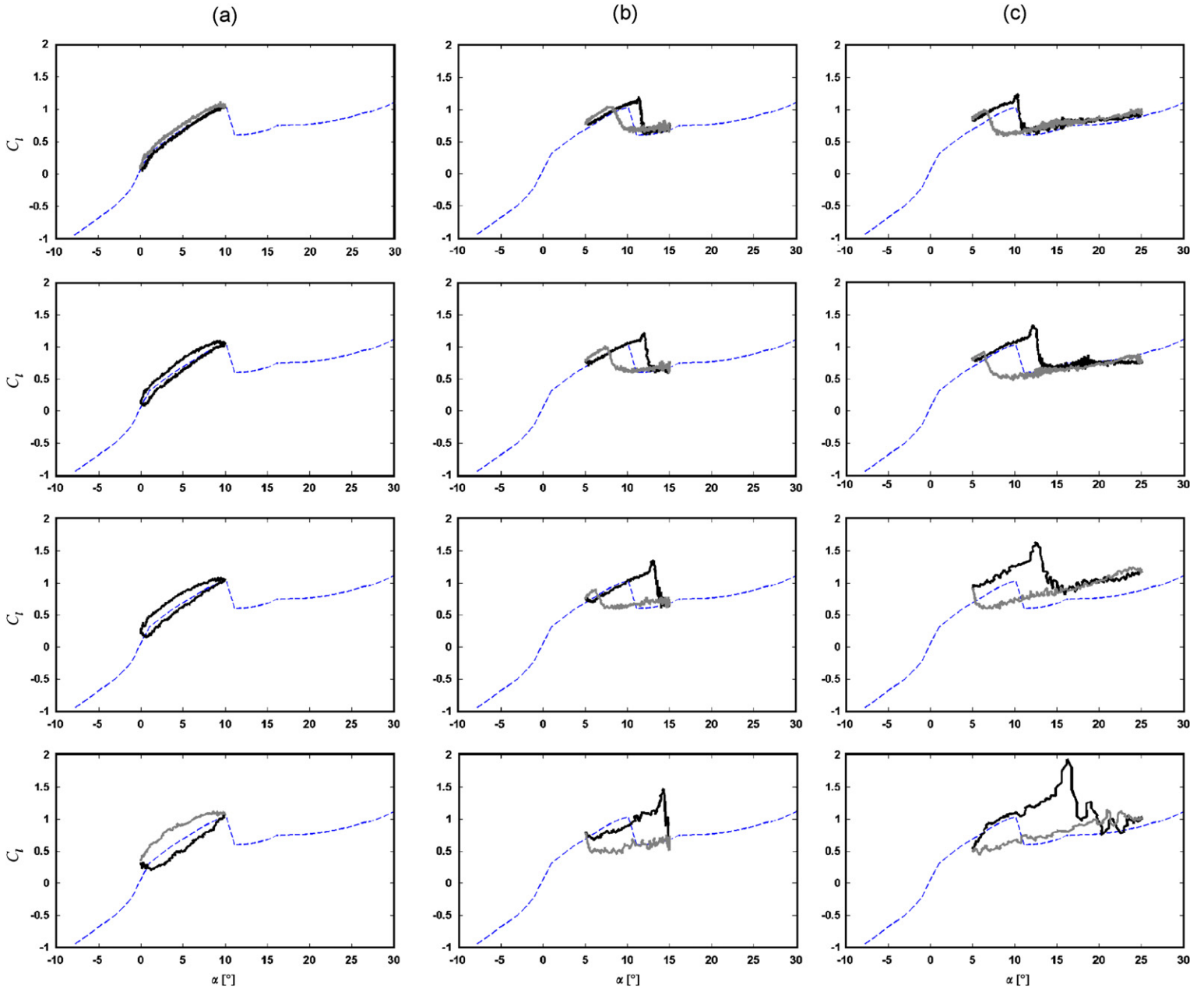


Fig. 6. Phase-averaged lift curve for Cases 2, 3, and 5 with different $k$: ▬▬, pitching up; ———, pitching down; – – – –, steady lift curve.

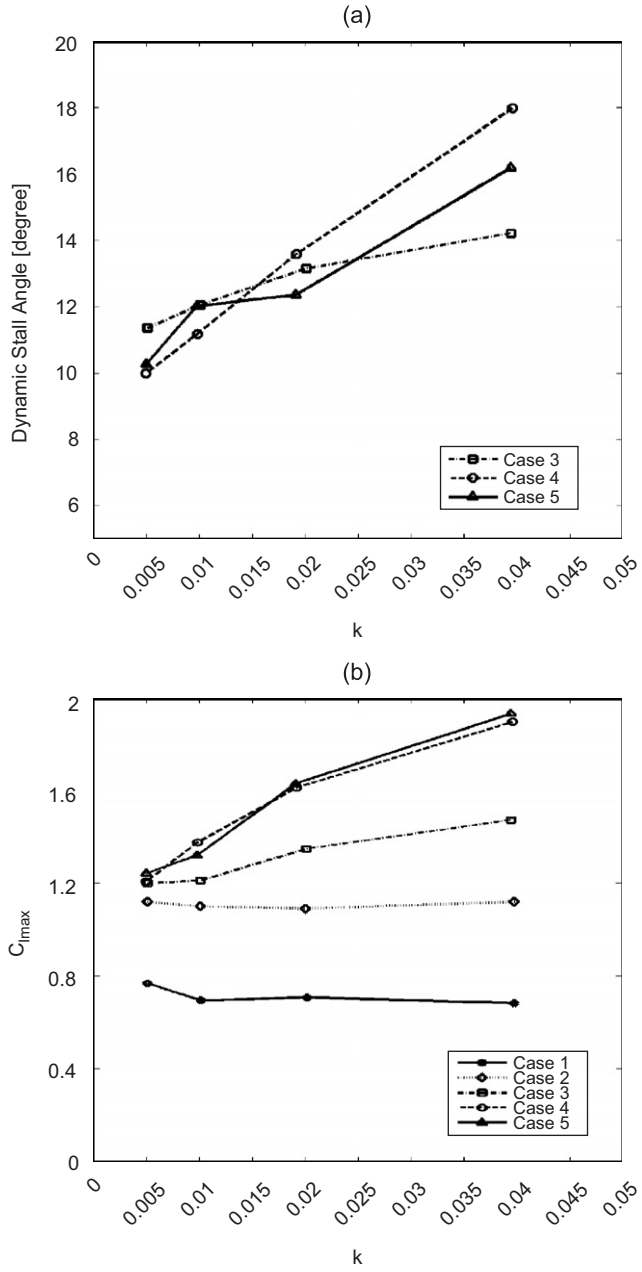


Fig. 7. Effect of reduced frequency $k$ on (a) dynamic stall angle and (b) maximum lift.

$C_{l\max}$ where $\alpha_{amp}$ increases $C_{l\max}$ for all $k$ examined. On the other hand, $\alpha_{amp}$ only contributes to an increase in the dynamic stall angle beyond $k = 0.02$.

### 3.5. Spectral analysis of unsteady lift and drag

The dynamic stall behavior as exemplified by the lift curve during one cycle of pitching has been examined above. In the following, different data analysis techniques are used to analyze the lift and drag signal to further understand their features related to the stall behavior.

The power spectral density (PSD) functions of the lift and drag signals are calculated using an FFT-based estimation method (Marple, 1987) implemented by the MATLAB signal processing toolbox. The results for Cases 2, 4, and 5 are shown in Fig. 8(a) and (b); they represent the pre-stall, light-stall, and full-stall case, respectively. Fig. 8(a) gives the lift results, while Fig. 8(b) shows the drag behavior. The spectra of Cases 1 and 3 are similar to those of Cases 2 and 4, thus, they are not shown.

In order to facilitate easy comparison of PSD functions of various test cases, all calculated PSD functions are normalized by the total power within the period of time examined, that is, $P = P/\int_0^\infty P(f)\,\mathrm{d}f$, where the frequency $f$ is normalized by the pitching frequency of that particular case. Only the frequency contents below $f = 10$ are plotted, since the power is found to be mainly concentrated in this range.

From the PSD plots, it is seen that the component at the fundamental pitching frequency is dominant, except for the lift of Case 5 at a $k = 0.005$. This is expected, since the airfoil undergoes forced-pitching oscillation in the experiment, and energy transferred to the airfoil should be mainly concentrated in this frequency. Moreover, it can be seen that both the lift and the drag have some higher order harmonics of the fundamental pitching frequency. This suggests that there exists nonlinear interaction between the airfoil and the surrounding flow, which renders energy transfer from the fundamental frequency to higher harmonics. For the pre-stall case (Case 2), the higher harmonics of the lift are not significant, and the higher harmonics of the drag are mainly at the second, third, and eighth order. For the light-stall case (Case 4), higher harmonics of the lift become significant at the second, third, and fifth orders, while the higher harmonics of the drag become insignificant. For the full-stall case (Case 5), higher harmonics of the lift are concentrated at the second, fifth, and eighth orders, while the drag is mainly at its fundamental frequency. In general, higher harmonics of the lift become significant with the increment of the degree of dynamic stall, while an opposite trend is observed for the drag.

In order to quantitatively demonstrate the energy partition between the fundamental frequency component and the higher harmonics, the energy partition of the fundamental component is calculated, which is defined as

$$P_{f1} = \frac{\int_{0.5}^{1.5} P(f)\,\mathrm{d}f}{\int_0^\infty P(f)\,\mathrm{d}f}. \tag{2}$$

Thus defined, $P_{f1}$ could be considered as an indicator of nonlinearity of the entity examined. When $P_{f1}$ is close to unity, most of the energy is concentrated at the fundamental frequency, implying the entity is linear; otherwise, the entity is nonlinear.

The computed results of energy partition of the fundamental component of the lift and drag signals are shown in Fig. 9. Consistent with the spectral analysis results, the lift and the drag show opposite trends when the degree of dynamic stall increases. For the lift, $P_{f1} \approx 1$ for the pre-stall case (Case 2), and varies between 0.1 and 0.6 for the light-stall and the full-stall cases (Cases 4 and 5). This suggests that the nonlinearity of the lift increases when the airfoil approaches into the dynamic stall regime. Increasing $k$ appears to enhance the nonlinearity. For the drag, the nonlinearity increases with the increment of the degree of dynamic stall, and increasing $k$ appears to enhance the linearity. When the lift or the drag is nonlinear, the influence of $k$ becomes significant.

### 3.6. Nonlinear correlation analysis of unsteady lift and drag

It is clear from the above analysis that energy is partitioned to different higher harmonics at different stages of dynamic stall. This feature is further studied by nonlinear correlation analysis. In the nonlinear correlation analysis, higher order coherence functions between any two of $\alpha$, $C_l$, and $C_d$ are calculated from their high-order spectra, given by Nikias and Petropulu (1993) as

$$\gamma_k(s_1, s_2; \omega_1, \omega_2, \ldots, \omega_{k-1}) = \frac{|P_k^{s_1 s_2}(\omega_1, \omega_2, \ldots, \omega_{k-1})|}{[P_2^{s_1 s_1}(\omega_1) \times P_2^{s_1 s_1}(\omega_2) \times \cdots \times P_2^{s_1 s_1}(\omega_{k-1}) \times P_2^{s_2 s_2}(\omega_1 + \omega_2 + \cdots + \omega_{k-1})]^{1/2}}, \tag{3}$$

where $s_1$ and $s_2$ are two entities whose correlation is to be analyzed, $k = 2, 3, 4, \ldots$, represents the order of the coherence function, and $P_k^{s_1 s_2}(\omega_1, \omega_2, \ldots, \omega_{k-1})$ is the $k$th order cross-spectral density function of $s_1$ and $s_2$. When $s_1 = s_2$, it becomes the $k$th order auto (power)—spectral density function.

Theoretically, if $\gamma_k(s_1, s_2; \omega_1, \omega_2, \ldots \omega_{k-1}) = 1$, then the phase coupling relationship exists between the harmonic component of the entity $s_2$ at $\omega_{\mathrm{sum}} = \omega_1 + \omega_2 + \cdots + \omega_{k-1}$ and the harmonic components of the entity $s_1$ at $\omega = \omega_1, \omega_2, \ldots, \omega_{k-1}$. However, due to computational error, the value of the coherence function could not be perfectly unity. Hence, a threshold of $\gamma_k(s_1, s_2; \omega_1, \omega_2, \ldots, \omega_{k-1}) = 0.97$ is set for the correlation to hold. When $\gamma_k(s_1, s_2; \omega_1, \omega_2, \ldots, \omega_{k-1}) < 0.97$, it is considered that the correlation between the two entities is not significant enough and could be neglected.

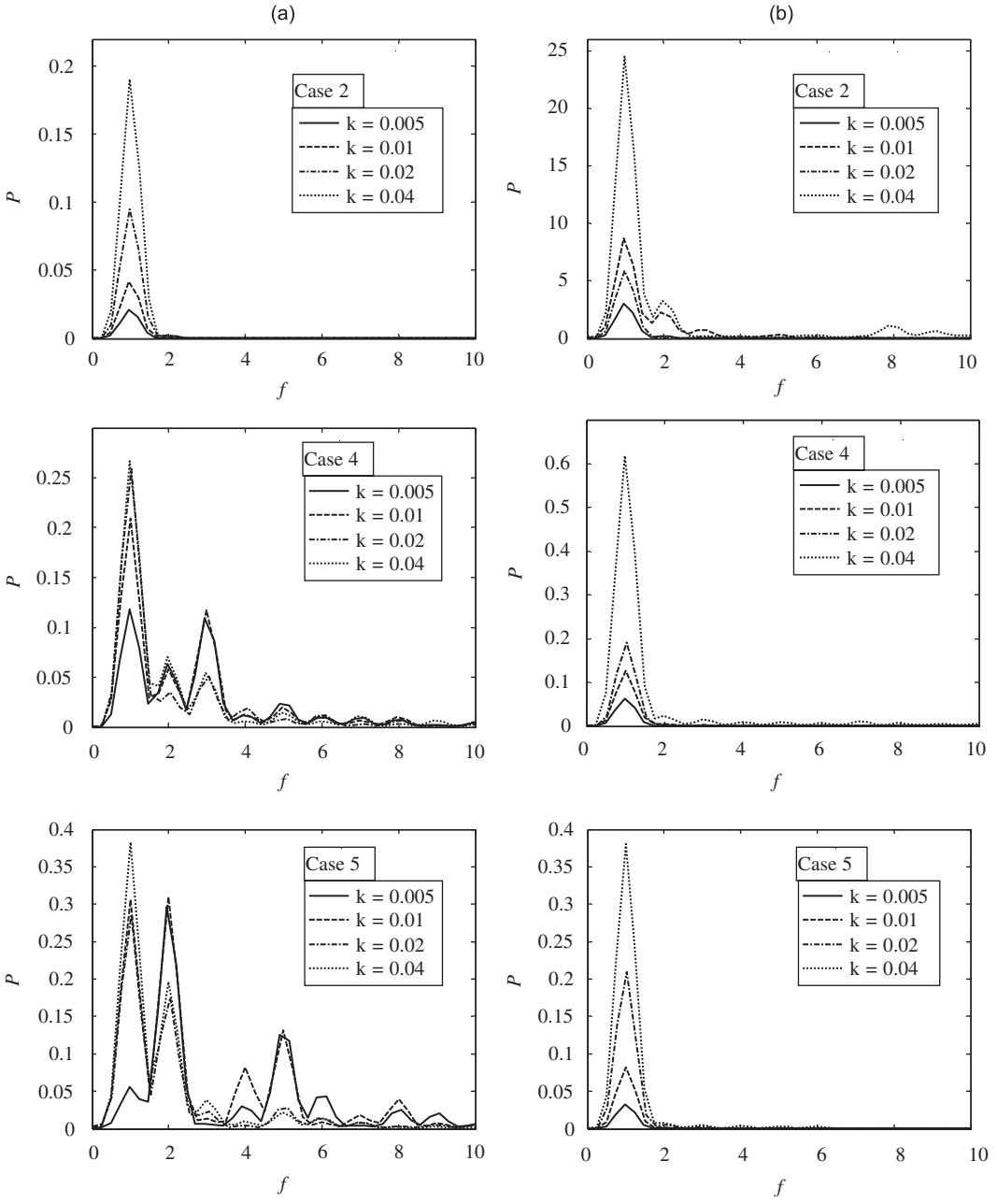


Fig. 8. Power spectral density (PSD) functions of the lift and drag data for three representative cases: the pre-stall case (Case 2), the light-stall case (Case 4), and the full-stall case (Case 5): (a) lift and (b) drag.

In the present analysis, only the coherence functions up to the fourth order (tri-linear) are considered. Three sets of data, that is, Case 2 at $k = 0.04$, Case 4 at $k = 0.04$, and Case 5 at $k = 0.005$, are selected to represent the pre-stall, light-stall, and full-stall case, respectively. A low value of $k$ for Case 5 is chosen since at this $k$, the nonstationary feature of the data is most significant, and appropriate for later study of nonstationarity.

The computed coherence functions are listed in Tables 1, 2, and 3, respectively. For the pre-stall case, $C_l$ and $\alpha$, $C_d$ and $\alpha$, $C_l$ and $C_d$ are all linearly correlated at the fundamental (pitching) frequency with no significant nonlinear interaction between them exists. This is reasonable, since the interaction is expected to be linear in the pre-stall case; the dynamic phenomenon is consistent with the linear airfoil theory; consequently, the $C_l$ slope is $2\pi$. It is interesting to note

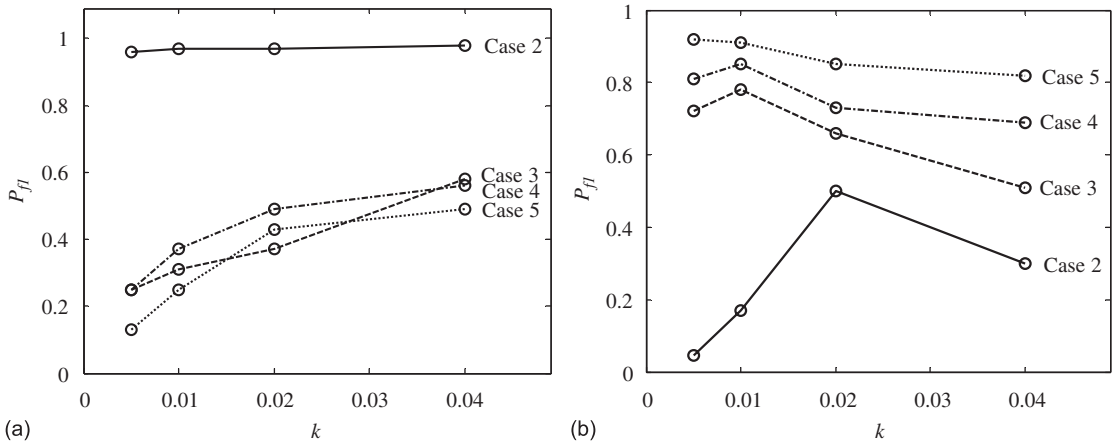


Fig. 9. Effect of reduced frequency $k$ on energy partition of the fundamental (pitching) frequency component of the fluid force: (a) lift and (b) drag.

Table 1
Coherence functions among $\alpha$, $C_l$, and $C_d$, for Case 2 (pre-stall case)

| | $\gamma_2(f)$ | $\gamma_3(f_1,f_2)$ | $\gamma_4(f_1,f_2,f_3)$ |
|---|---|---|---|
| $(C_l, \alpha)$ | $\gamma_2(1) = 1.00$ | $<0.97$ | $<0.97$ |
| $(C_d, \alpha)$ | $\gamma_2(1) = 0.99$ | $<0.97$ | $<0.97$ |
| $(C_l, C_d)$ | $\gamma_2(1) = 0.99$ | $<0.97$ | $<0.97$ |
| $(C_d, C_l)$ | $\gamma_2(1) = 0.99$ | $<0.97$ | $<0.97$ |

that the coherence functions $\gamma_n$ are in general not symmetric with harmonic components for $n \geqslant 3$. The loss of symmetry of $\gamma_n$ provides further evidence for the nonlinear coupling between $\alpha$, $C_l$ and $C_d$ of the pitching airfoil.

For the light-stall case, $C_l$ and $\alpha$, $C_d$ and $\alpha$, $C_l$ and $C_d$ are also linearly correlated at the fundamental (pitching) frequency, and $C_l$ and $C_d$ are linearly correlated at several higher harmonics. Moreover, nonlinear correlation exists between $C_l$ and $C_d$. This suggests that the higher order harmonics of $C_l$ and $C_d$ in this light-stall case are more likely due to the interaction between $C_l$ and $C_d$ rather than the direct effect of the pitching motion of the airfoil. It should be noted that the energy partition of the fundamental frequency component $P_{f1}$ of the lift or drag in this case is neither close to unity nor to zero, and this may be due to the interaction between $C_l$ and $C_d$ as indicated by the correlation analysis results.

For the full-stall case, $C_l$ and $\alpha$, $C_d$ and $\alpha$, are linearly correlated at the fundamental (pitching) frequency, but $C_l$ and $C_d$ are not. There is bi-linear correlation between $C_l$ and $\alpha$, $C_d$ and $\alpha$, but tri-linear correlation exists only between $C_d$ and $\alpha$. Moreover, $C_l$ and $C_d$ are bi-linearly correlated while $C_d$ and $C_l$ are tri-linearly correlated. This implies that the interaction in the full-stall case is very complicated, including both linear and nonlinear terms.

### 3.7. Nonstationary features of unsteady lift and drag

In the previous spectral analysis, an FFT-based method is used to estimate the PSD function, which assumes the data is stationary; hence possible power variation of the data with time is lost. A time-frequency analysis method has to be used if the features of the data were to be fully recovered.

In the present study, the continuous wavelet analysis is carried out to investigate whether the lift and drag signal have time-variant features. The continuous wavelet transform (CWT) is defined as

$$\mathrm{CWT}(s,\tau) = \frac{1}{\sqrt{s}} \int_{-\infty}^{\infty} w(t) \psi^* \left( \frac{t-\tau}{s} \right) \mathrm{d}t, \tag{4}$$

where $w(t)$ is the data to be analyzed, $\psi(t)$ is called the mother wavelet, $s$ is the scaling factor, and $\tau$ is the translating factor. The superscript "*" represents the complex conjugate.

Table 2
Coherence functions among $\alpha$, $C_l$, and $C_d$, for Case 4 (light-stall case)

| | $\gamma_2(f)$ | $\gamma_3(f_1,f_2)$ | $\gamma_4(f_1,f_2,f_3)$ |
|---|---|---|---|
| $(C_l, \alpha)$ | $\gamma_2(1) = 1.00$ | $<0.97$ | $<0.97$ |
| $(C_d, \alpha)$ | $\gamma_2(1) = 1.00$ | $<0.97$ | $<0.97$ |
| $(C_l, C_d)$ | $\gamma_2(1) = 1.00$ | $\gamma_3(1,1) = 0.99$ | $\gamma_4(1,1,1) = 0.99$ |
| | $\gamma_2(2) = 0.99$ | $\gamma_3(1,2) = 0.99$ | $\gamma_4(1,1,2) = 0.99$ |
| | $\gamma_2(3) = 0.98$ | $\gamma_3(1,3) = 0.99$ | $\gamma_4(1,1,3) = 0.99$ |
| | $\gamma_2(4) = 0.99$ | $\gamma_3(1,4) = 0.97$ | $\gamma_4(1,1,7) = 0.98$ |
| | $\gamma_2(6) = 0.99$ | $\gamma_3(1,5) = 0.98$ | $\gamma_4(1,2,2) = 0.99$ |
| | $\gamma_2(8) = 0.98$ | $\gamma_3(1,6) = 0.97$ | $\gamma_4(1,2,3) = 0.99$ |
| | $\gamma_2(9) = 0.97$ | $\gamma_3(2,2) = 0.99$ | $\gamma_4(1,2,5) = 0.99$ |
| | | $\gamma_3(2,3) = 0.97$ | $\gamma_4(1,2,6) = 0.98$ |
| | | $\gamma_3(2,4) = 0.97$ | $\gamma_4(1,3,5) = 0.99$ |
| | | $\gamma_3(2,5) = 0.98$ | $\gamma_4(2,2,2) = 0.99$ |
| | | $\gamma_3(2,6) = 0.98$ | $\gamma_4(2,2,3) = 0.98$ |
| | | $\gamma_3(2,7) = 0.98$ | $\gamma_4(2,2,5) = 0.99$ |
| | | | $\gamma_4(2,2,3) = 0.99$ |
| | | | $\gamma_4(3,3,3) = 0.97$ |
| $(C_d, C_l)$ | $\gamma_2(1) = 1.00$ | $\gamma_3(1,1) = 1.00$ | $\gamma_4(1,1,1) = 0.99$ |
| | $\gamma_2(2) = 0.99$ | $\gamma_3(1,2) = 0.97$ | $\gamma_4(1,1,3) = 0.99$ |
| | $\gamma_2(3) = 0.98$ | $\gamma_3(1,3) = 0.98$ | $\gamma_4(1,1,5) = 0.98$ |
| | $\gamma_2(4) = 0.99$ | $\gamma_3(1,4) = 0.97$ | $\gamma_4(1,2,1) = 0.99$ |
| | $\gamma_2(6) = 0.99$ | $\gamma_3(1,5) = 0.98$ | $\gamma_4(1,2,2) = 0.98$ |
| | $\gamma_2(8) = 0.98$ | $\gamma_3(1,7) = 0.97$ | $\gamma_4(1,2,3) = 0.98$ |
| | $\gamma_2(9) = 0.97$ | $\gamma_3(1,8) = 0.98$ | $\gamma_4(1,2,4) = 0.98$ |
| | | $\gamma_3(2,2) = 0.97$ | $\gamma_4(1,2,5) = 0.98$ |
| | | $\gamma_3(2,7) = 0.97$ | $\gamma_4(1,2,6) = 0.98$ |
| | | $\gamma_3(3,5) = 0.97$ | $\gamma_4(1,3,1) = 0.99$ |
| | | $\gamma_3(3,6) = 0.97$ | $\gamma_4(1,3,2) = 0.98$ |
| | | | $\gamma_4(1,3,3) = 0.97$ |
| | | | $\gamma_4(1,3,4) = 0.98$ |
| | | | $\gamma_4(1,3,5) = 0.97$ |
| | | | $\gamma_4(3,3,2) = 0.98$ |
| | | | $\gamma_4(4,3,2) = 0.97$ |
| | | | $\gamma_4(5,2,2) = 0.98$ |

Table 3
Coherence functions among $\alpha$, $C_l$, and $C_d$, for Case 5 (full-stall case)

| | $\gamma_2(f)$ | $\gamma_3(f_1,f_2)$ | $\gamma_4(f_1,f_2,f_3)$ |
|---|---|---|---|
| $(C_l, \alpha)$ | $\gamma_2(1) = 0.99$ | $\gamma_3(1,2) = 0.97$ | $<0.97$ |
| | | $\gamma_3(2,2) = 0.99$ | |
| | | $\gamma_3(4,5) = 0.97$ | |
| $(C_d, \alpha)$ | $\gamma_2(1) = 0.99$ | $\gamma_3(1,1) = 1.00$ | $\gamma_4(1,1,1) = 1.00$ |
| | | $\gamma_3(1,2) = 0.97$ | |
| $(C_l, C_d)$ | $<0.97$ | $\gamma_3(2,2) = 0.98$ | $<0.97$ |
| | | $\gamma_3(2,6) = 0.98$ | |
| $(C_d, C_l)$ | $<0.97$ | $<0.97$ | $\gamma_4(1,1,1) = 1.00$ |
| | | | $\gamma_4(5,1,1) = 0.98$ |

Wavelet analysis decomposes a set of data into the time-frequency domain, thus is able to resolve power variation of individual frequency components of the data with time. The result of wavelet analysis is presented in the form of a spectrogram, which is defined as $P_{\mathrm{CWT}} = \left|\mathrm{CWT}(s,\tau)\right|^2$ and can be regarded as a series of instantaneous PSD functions in the time-frequency domain. In the wavelet analysis, the temporal scaling factor $s$ is used, rather than the normal

frequency employed in conventional Fourier analysis. In order to interpret the results of wavelet analysis in the conventional way, the scaling factor $s$ needs to be converted into an equivalent Fourier frequency, $f_{eq}$.

In the present analysis, the CWT with the Morlet wavelet, $\psi(t) = \pi^{-1/4}\, e^{i\omega_o t}\, e^{-t^2/2}$, as mother wavelet is used as suggested by Farge (1992). For the Morlet wavelet, the relation between the equivalent Fourier frequency and the scaling factor is given by $f_{eq} = 1/1.03\,s$. The CWT of the measured force data is performed using the algorithm developed by Torrence and Combo (1998). Furthermore, in order to facilitate easy comparison of the wavelet spectrograms of various test cases in the present experiment, all calculated wavelet spectrograms are normalized by the total power within the period of time examined, i.e., $P_{CWT}(t,f) = P_{CWT}(t,f)/\iint P_{CWT}(t,f)\,dt\,df$, where the frequency $f_{eq}$ and the time $\tau$ are normalized by the pitching frequency and the sampling time, respectively, of that particular case.

The three sets of data invoked in nonlinear correlation analysis are used in the present wavelet analysis. The computed spectrograms are illustrated in Fig. 10(a)–(c), respectively. For the pre-stall case (Case 2 with $k = 0.04$), the spectrograms essentially show no variation within one cycle and over the 10 cycles of oscillation examined. A persistent peak shows up at $f = 1$ (Fig. 10(a)) as expected. This shows that while energy is input into the airfoil at $f = 1$, the lift at $f = 1$ dominates the spectra. In addition, this peak at $f = 1$ persists during the entire pitching cycle and the magnitude of the peak remains unchanged. Thus, the signal is typical of that observed for the lift measured ahead of $\alpha_{ss}$, is stationary and there is no energy transfer between frequencies. The same is true for the drag, except for a small stationary peak at $f = 2$.

For the light-stall case (Case 4 with $k = 0.04$), persisting peaks are observed at $f = 1$ and at $f = 2$ for both the lift and the drag (Fig. 10(b)). At a frequency near $f = 3$ of the lift, higher power is also observed but this peak is not present for all 10 cycles of the time series examined. In general, this case is still a stationary one, with a weak nonstationarity in the third harmonic of the lift.

For the full-stall case (Case 5 at $k = 0.005$), persisting peaks are observed at $f = 1$ and at $f = 2$ for the lift and at $f = 1$ for the drag (Fig. 10(c)). For the lift, however, at a frequency band covering $f = 4$–$6$, high power is observed but it is not present in each of the 10 cycles of the time series examined. The amplitude of the spectrogram appears to vary with time periodically, at the pitching frequency. Another frequency band covering $f = 8$–$9$ also show nonstationary behavior, but at a rather weak power level. These features indicate that the lift in Case 5 is nonstationary at higher harmonics, while the drag appears to be stationary.

In order to further illustrate the nonstationarity of the lift in the dynamic stall regime, slices of the spectrograms at selected instantaneous time are presented to give the PSD with frequency at that time. Temporal variation of the spectrum can thus be examined in detail. The power spectra at nine selected instantaneous time during one cycle of oscillation for the light-stall case (Case 4 at $k = 0.04$) and the full-stall case (Case 5 at $k = 0.005$) are shown in Figs. 11 and 12, respectively. Each of the nine selected times are separated by one-eighth of a period within each cycle of oscillation.

For the light-stall case, peaks are observed at $f = 1$–$3$ at all selected times within one cycle of oscillation (Fig. 11). While the peaks at $f = 1$ and 2 appear to be time-invariant, the peak at $f = 3$ becomes less and less prominent as $\alpha$ increases during upstroke, but regains its sharpness in the down-stroke. This variation is evidence that the third harmonic of the lift is nonstationary within one cycle of oscillation of the airfoil.

For the full-stall case, prominent peaks are also observed at $f = 1$–$3$ at all selected times within one cycle of oscillation (Fig. 12). At the minimum $\alpha$, a pronounced peak is found at around $f = 5$, while a smaller peak is observed between $f = 8$ and 9. As $\alpha$ increases, both peaks lose their magnitude and at $\alpha = 15.1$, the peak between $f = 8$ and 9 completely disappears while the peak at $f = 5$ remains but with a smaller magnitude. As $\alpha$ continues to increase, new peaks are observed between $f = 3$ and 4, and near $f = 7$. Again, these variations clearly show that higher order harmonics of the lift are nonstationary even within one cycle of oscillation. The degree of nonstationarity is clearly higher than that of the light-stall case.

### 3.8. Energy partition based on CWT results

In an attempt to have an integrated understanding of nonlinear and nonstationary features of the lift and drag of the airfoil in the dynamic stall regime, energy partitions of the fundamental frequency components of the lift and the drag are calculated using the CWT results. This energy partition result is different from the previous one since it gives time-variant features, as shown by its definition, written as

$$P_{f1}(t) = \frac{\int_{0.5}^{1.5} P_{CWT}(t,f)\,df}{\int_{0}^{\infty} P_{CWT}(t,f)\,df}. \tag{5}$$

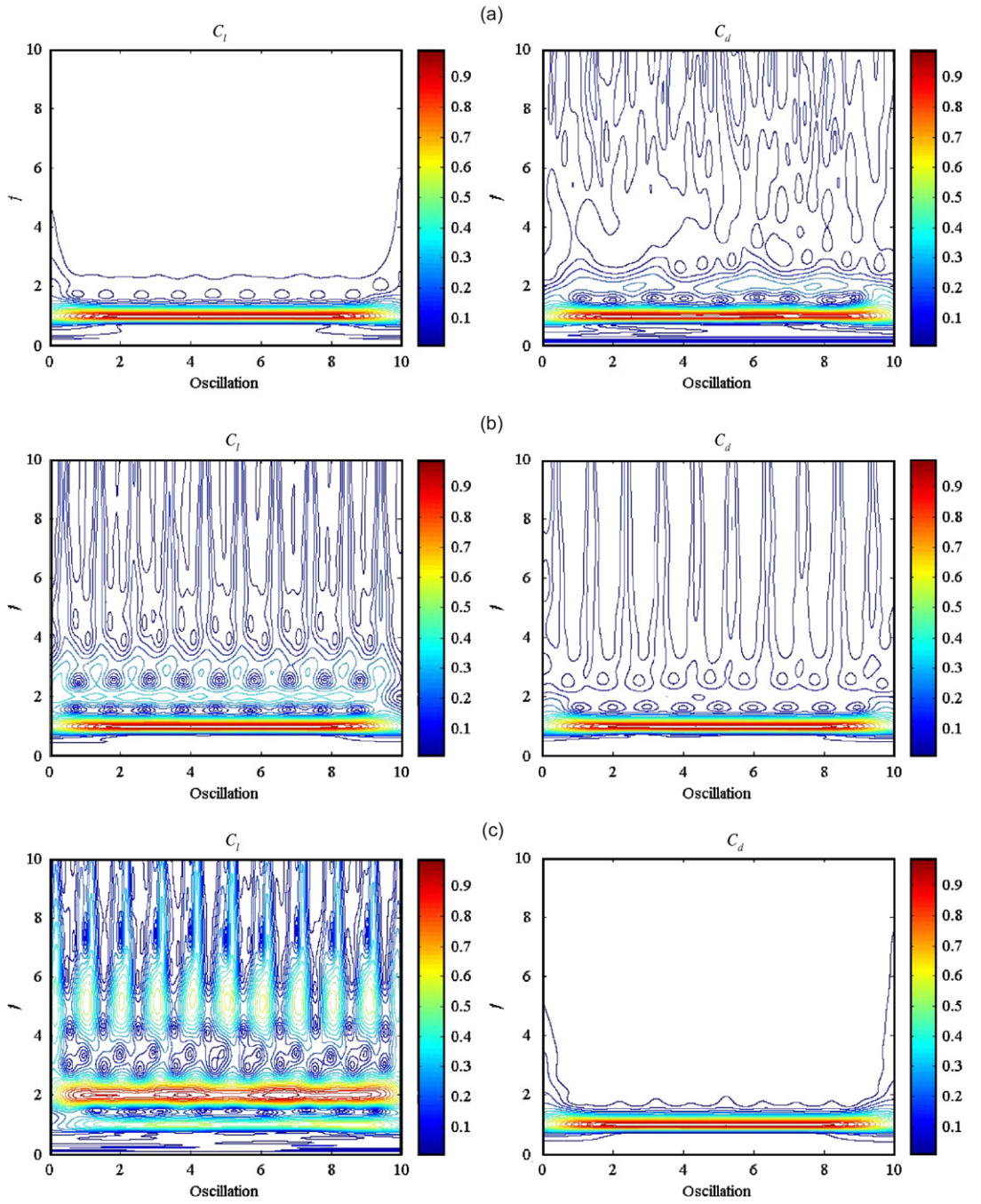


Fig. 10. Spectrogram of the wavelet analysis of 10 cycles of oscillation of the lift and the drag time series for Cases 2, 4, and 5: (a) Case 2; (b) Case 4; and (c) Case 5.

In Fig. 13 are shown the energy partition results of the three representative cases. The results are averaged over 10 cycles of pitching, so that only the variation of energy partition within one cycle is illustrated.

For the pre-stall case (Fig. 13(a)), the energy partition of lift is close to unity and appears to be stationary, while that of drag is around 0.4 and shows slight fluctuation with time. This means that the lift in the pre-stall case is a linear and stationary process, while the drag has slight nonlinear and nonstationary behavior.

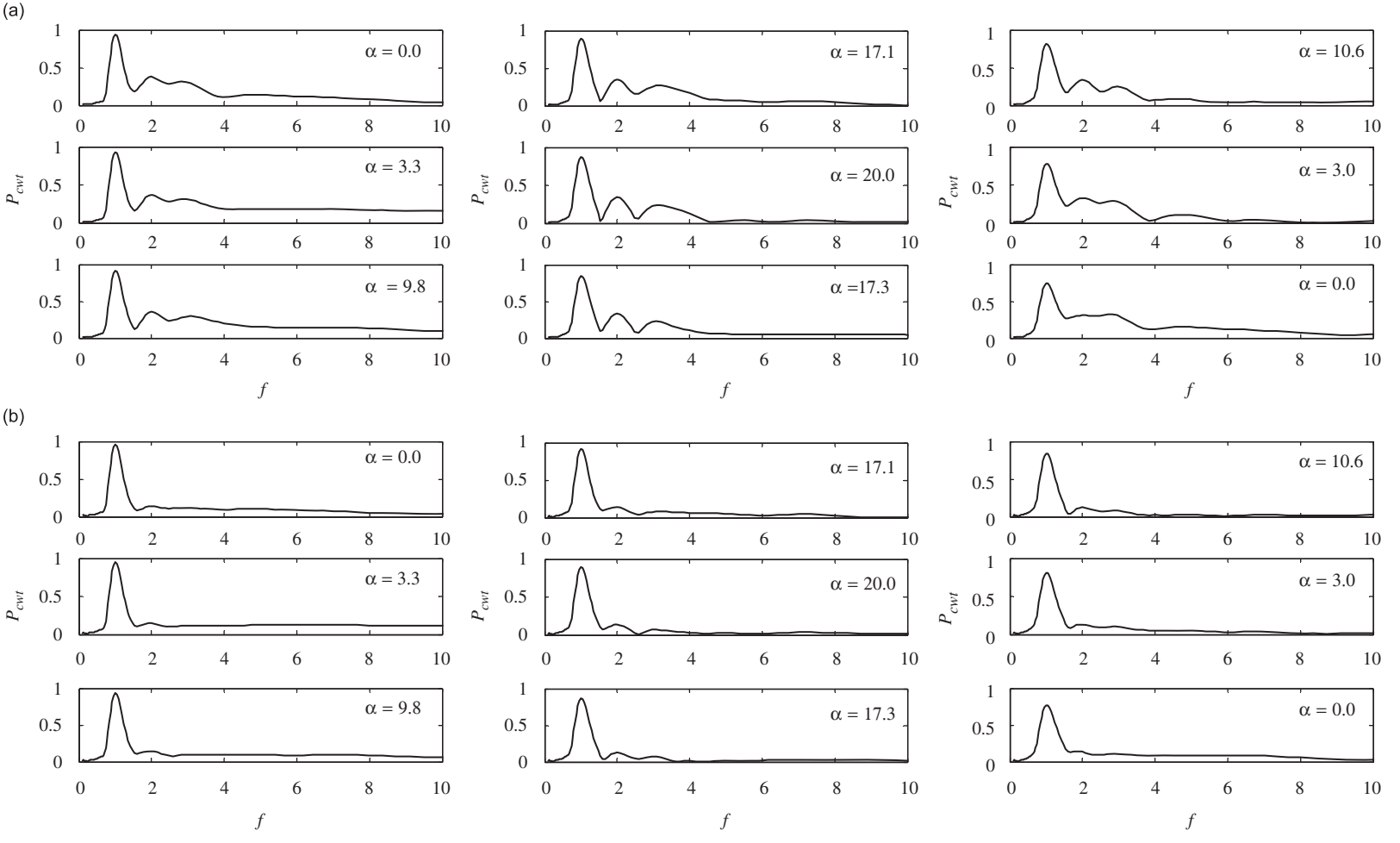


Fig. 11. Power spectra at selected times for Case 4 with $\alpha = 10^\circ + 10^\circ \sin(\omega t)$, and $k = 0.04$: (a) lift and (b) drag.

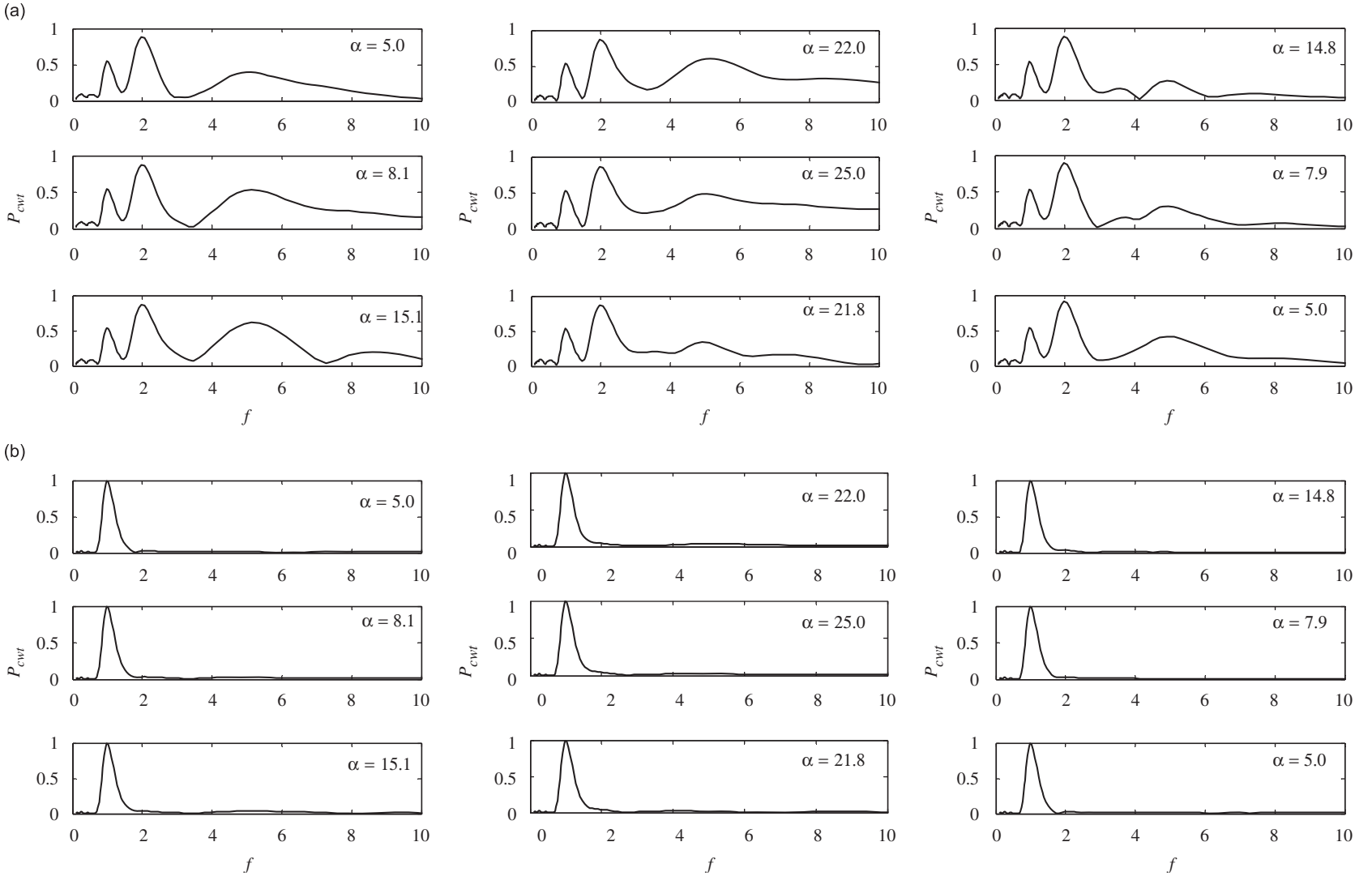


Fig. 12. Power spectra at selected times for Case 5 with $\alpha = 15^\circ + 10^\circ \sin(\omega t)$ and $k = 0.005$: (a) lift and (b) drag.

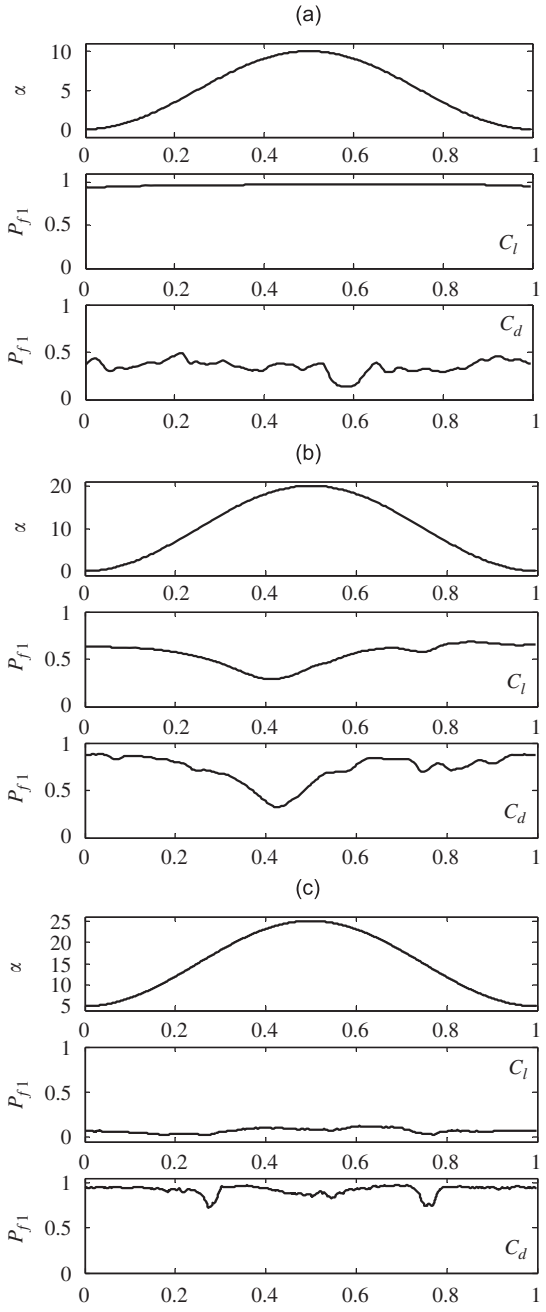


Fig. 13. Energy partition of the fundamental (pitching) frequency component of the lift and drag force within one cycle of pitching: (a) Case 2; (b) Case 4; and (c) Case 5.

For the light-stall case (Fig. 13(b)), the energy partition of lift drops to a value around 0.5, and appears to be slightly nonstationary, with a drop to the minimum value when the airfoil approaches its maximum pitching angle. The energy partition of drag, on the contrary, increases to a value close to unity, except for a drop to 0.4 when the airfoil approaches the maximum pitching angle. This suggests that when the airfoil is in the light-stall regime, the lift approaches nonlinear behavior, while the drag approaches linearity. A nonstationary behavior also appears, that is, both lift and drag tend to be more nonlinear when the airfoil pitches to its maximum angle of attack. The nonlinear interaction between lift and drag, as illustrated by the coherence functions given in Table 2, may be strong at this maximum pitching angle.

For the full-stall case, the energy partition of lift drops further to a value close to zero, implying that most of the energy is transferred to higher harmonics. The energy partition appears to be stationary. The energy partition of drag increases to a value very close to unity, but shows two drops when the airfoil passes its mean pitching angle.

These results essentially corroborate the findings on nonlinearity and nonstationarity of the lift and drag signals based on nonlinear correlation analysis, spectral analysis and energy partition derived from PSD results. Therefore, this is a viable alternative for nonlinear and nonstationary analysis of unsteady signals.

## 4. Conclusions

A piezoelectric load cell direct force measurement technique has been used to study the physics of dynamic stall at $\mathrm{Re} = 7.7 \times 10^4$. The static stall angle $\alpha_{ss}$ is determined to be approximately $10^\circ$ and the lift curve slope is determined to be $2\pi$. The measured $\alpha_{ss}$ is lower than that reported in the literature; however, the lower value is a consequence of early separation of the flow from the suction surface of the airfoil. Flow visualization provides supporting evidence to corroborate this conclusion.

Dynamic stall is created by pitching the airfoil at specified pitching reduced frequencies $k$, amplitude of pitching motion $\alpha_{amp}$, and the mean pitching angle $\alpha_{mean}$. Altogether, five different cases with four $k$ ranging from 0.005 to 0.04 are investigated. These five cases are chosen to cover the pre-stall, light-stall, and full-stall regime. At least two of the five cases investigated have the same $\alpha_{mean}$ but different $\alpha_{amp}$, and another two have the same $\alpha_{amp}$ but different $\alpha_{mean}$. This way, the effects of $k$, $\alpha_{amp}$, and $\alpha_{mean}$ can be examined. It is found that the dynamic stall angle is significantly affected by $k$; so is the maximum lift coefficient $C_{l\max}$. The dynamic stall angle increases with $k$ but the effect for the light-stall case is much milder compared to the full-stall case. A similar effect is also observed for $C_{l\max}$; however, $k$ essentially has no effect on $C_{l\max}$ in the pre-stall regime. On the other hand, $\alpha_{mean}$ has a slight effect on the dynamic stall angle but little or no effect on $C_{l\max}$, while $\alpha_{amp}$ has an effect on both the dynamic stall angle and $C_{l\max}$.

Various data analysis techniques are used to investigate nonlinear and nonstationary features of lift and drag in the stall regime, and the concept of energy partition is proposed for a quantitative demonstration of nonlinearity and nonstationarity. The classical FFT-based spectral analysis results reveal that in addition to the component at the fundamental pitching frequency, higher order harmonics are found, suggesting nonlinear interaction between the fluid force and the pitching motion of the airfoil, which gives rise to energy transfer from the fundamental component to higher harmonics. The energy partition of the fundamental frequency component is calculated using the classical spectral analysis results. It is found that the lift and the drag show opposite behavior when the airfoil undergoes transition from the pre-stall regime to the full-stall regime; the nonlinearity of the lift increases while that of the drag decreases. The effect of $k$ becomes significant when nonlinearity is strong.

Results of coherence functions up to the fourth order (tri-linear) between any two of the lift, the drag, and the pitching angle reveal that the interaction between the fluid force and the pitching motion is essentially linear in the pre-stall regime. Higher order harmonics are due to the interaction of the lift and the drag in the light-stall regime, while additional nonlinear interaction between the fluid force and the pitching motion is found in the full-stall regime.

CWT results indicate that the fundamental components of lift and drag are essentially stationary, but the higher order harmonics show certain nonstationary features, and the degree of nonstationarity increases with the degree of dynamic stall. Time-variant energy partition of the fundamental frequency component is calculated using the wavelet analysis results. It is shown that the nonstationarity of lift is significant in the light-stall regime and occurs when the airfoil approaches its maximum pitching angle. In the full-stall regime, the lift also appears to be nonstationary at higher harmonics, but its influence on energy transfer is slight. The drag shows nonstationarity in the pre-stall, light-stall, and full-stall regimes, and is most significant in the light-stall regime and occurs simultaneously with the lift. This synchronization may contribute to the nonlinear interaction between lift and drag as illustrated by the coherence functions. Furthermore, the nonstationarity of drag in the full-stall regime shows a different feature from that in the light-stall regime; it is significant when the airfoil passes the mean pitching angle.

## Acknowledgments

Support from the Research Grants Council of the HKSAR Government given under grant nos. PolyU5272/04E and PolyU1/02C is gratefully acknowledged.

## References

Albertson, J.A., Troutt, T.R., Siuru, W.D., Walker, J.M., 1987. Dynamic stall vortex development and the surface pressure field of a pitching airfoil. AIAA Paper 87-1333.

Baban, F., So, R.M.C., 1991. Recirculating flow behind and unsteady forces on finite-span circular cylinders in a cross-flow. Journal of Fluids and Structures 5, 185–206.

Baban, F., So, R.M.C., Otügen, M.V., 1989. Unsteady forces on circular cylinders in a cross-flow. Experiments in Fluids 7, 293–302.

Carr, L.W., 1998. Progress in analysis and prediction of dynamic stall. Journal of Aircraft 25, 6–17.

Carr, L.W., McAlister, K.W., McCroskey, W.J., 1977. Analysis of the development of dynamic stall based on oscillating airfoil experiments. NASA TN-D8382.

Conger, R.N., Ramaprian, B.R., 1994. Pressure measurements on a pitching airfoil in a water channel. AIAA Journal 32, 108–115.

Dickinson, M.H., Lehmann, F.-O., Sane, S.P., 1999. Wing rotation and the aerodynamic basis of insect flight. Science 284, 1954–1960.

Farge, M., 1992. Wavelet transforms and their applications to turbulence. Annual Review of Fluid Mechanics 24, 395–457.

Lam, K., Li, J.Y., So, R.M.C., 2003. Force coefficient and Strouhal number of four cylinders in cross flow. Journal of Fluids and Structures 18, 305–324.

Lam, K., Wang, F.H., Li, J.Y., So, R.M.C., 2004. Experimental investigation of the mean and fluctuating forces of wavy cylinders in a cross-flow. Journal of Fluids and Structures 19, 321–334.

Lau, Y.L., So, R.M.C., Leung, R.C.K., 2004. Flow-induced vibration of elastic slender structures in a cylinder wake. Journal of Fluids and Structures 19, 1061–1083.

Leishman, J.G., 2000. Principles of Helicopter Aerodynamics. Cambridge University Press, Cambridge.

Marple Jr., S.L., 1987. Digital Spectral Analysis with Applications. Prentice-Hall, New Jersey.

Martin, J.M., Empey, R.W., McCroskey, W.J., Caradonna, F.X., 1974. An experimental analysis of dynamic stall on an oscillating airfoil. Journal of the American Helicopter Society 19, 26–32.

Mary, I., Sagaut, P., 2002. Large eddy simulation of flow around an airfoil near stall. AIAA Journal 40, 1139–1145.

McAlister, K.W., Carr, L.W., McCroskey, W.J., 1978. Dynamic stall experiments on the NACA 0012 airfoil. NASA TP-100.

Nikias, C.L., Petropulu, A.P., 1993. Higher-Order Spectra Analysis—A Nonlinear Signal Processing Framework. Prentice-Hall, New Jersey.

Oshima, H., Ramaprian, B.R., 1992. Measurements of the velocity and vorticity fields around a pitching airfoil. AIAA Paper 92-2626.

Panda, J., Zaman, K.B.M.Q., 1992. Experimental investigation of the flowfield of an oscillating airfoil. AIAA Paper 92-2622.

Panda, J., Zaman, K.B.M.Q., 1994. Experimental investigation of the flowfield of an oscillating airfoil and estimation of lift from wake surveys. Journal of Fluid Mechanics 265, 65–95.

Piziali, R.A., 1994. 2-D and 3-D oscillating wing aerodynamics for a range of angles of attack including stall. NASA TM-4632.

Richter, A., Naudescher, E., 1976. Fluctuating forces on a rigid circular cylinder in confined flow. Journal of Fluid Mechanics 78, 561–576.

Savkar, S.D., So, R.M.C., Listzinger, T.A., 1980. Fluctuating lift and drag forces induced on large span bluff bodies in a turbulent crossflow. ASME HTD-9, pp. 19–26.

Sin, V.K., So, R.M.C., 1987. Local force measurements on finite-span cylinders in a cross-flow. Journal of Fluids Engineering 109, 136–143.

So, R.M.C., Savkar, S.D., 1981. Buffeting forces on rigid circular cylinders in cross flows. Journal of Fluid Mechanics 105, 397–425.

So, R.M.C., Liu, Y., Cui, Z.X., Zhang, C.H., Wang, X.Q., 2005. Three-dimensional wake effects on flow-induced forces. Journal of Fluids and Structures 20, 373–402.

Torrence, C., Combo, G.P., 1998. A practical guide to wavelet analysis. Bulletin of the American Meteorological Society 79, 61–78.

Tsang, K.Y.K., 2006. Direct Force Measurements of a two-dimensional airfoil undergoing dynamic stall. M.Phil. Thesis, The Hong Kong Polytechnic University, Hong Kong.

Walker, J.M., Helin, H.E., Chou, D.C., 1985. Unsteady surface pressure measurements on a pitching airfoil. AIAA Paper 85-0532.

Wernert, P., Geissler, W., Raffel, M., Kompenhans, J., 1996. Experimental and numerical investigations of dynamic stall on a pitching airfoil. AIAA Journal 34, 982–989.

White, F.M., 1979. Fluid Mechanics. McGraw-Hill Book Company, New York.

Zaman, K.B.M.Q., McKinzie, D.J., Rumsey, C.L., 1989. A natural low-frequency oscillation of the flow over an airfoil near stalling conditions. Journal of Fluid Mechanics 202, 403–442.